A Self-Powered Wearable Sensor for Continuous Wireless Sweat Monitoring

Yansong Gai, Engui Wang, Minghao Liu, Lirong Xie, Yuan Bai, Yuan Yang, Jiangtao Xue, Xuecheng Qu, Yuan Xi, Linlin Li, Dan Luo, and Zhou Li**

Wireless wearable sweat analysis devices can monitor biomarkers at the molecular level continuously and in situ, which is highly desired for personalized health care. The miniaturization, integration, and wireless operation of sweat sensors improve the comfort and convenience while also bringing forward new challenges for power supply technology. Herein, a wireless self-powered wearable sweat analysis system (SWSAS) is designed that effectively converts the mechanical energy of human motion into electricity through hybrid nanogenerator modules (HNGMs). The HNGM shows stable output characteristics at low frequency with a current of 15 mA and a voltage of 60 V. Through real-time on-body sweat analysis powered by HNGM, the SWSAS is demonstrated to selectively monitor biomarkers (Na^+ and K^+) in sweat and wirelessly transmit the sensing data to the user interface via Bluetooth.

1. Introduction

The rapid development of wearable electronic technology provides infinite possibilities for personalized health cares.[1–5] As one of them, wireless wearable sweat monitoring devices can monitor biomarkers in a non-invasive, real-time, and continuous manner at the molecular level.[6–10] A multitude of health-related biomarkers are contained in sweat such as metabolites, electrolytes, protein, amino acids, hormones, and drugs.[11–14] Continuous monitoring of these biomarkers can provide a strong data basis for disease diagnosis, health management, drug abuse detection, and exercise performance optimization.[13,15] For example, the Cl^- concentration in sweat is already a clinical standard for rapid screening of cystic fibrosis,[16,17] and the Na^+ and K^+ concentrations in sweat reflect the electrolyte balance of the athlete's body.[18] Continuous data acquisition, processing, and wireless transmission set high demands on energy consumption. Up to now, rigid batteries like lithium-ion batteries have been the primary power source for most wearable electronics. Although the flexibility and miniaturization of batteries have expanded their applications in wearable electronics, they are still limited by frequent charging and replacement.[2,19,20] As an alternative to batteries, the powering technologies of near-field communication (NFC),[17,21] thermoelectric generator,[22] biofuel cell,[23,24] and solar cell[25,26] have been developed for wearable electronics. Unfortunately, these powering technologies are still unable to meet the needs of wearable electronics due to various limitations, such as short operation distance (NFC), low conversion efficiency (thermoelectric generators), unstable power outputs (biofuel cell), and environmental restrictions (solar cell).[20,27]

Considering that the human body sweats mostly in the scene of strenuous exercise, it may be an ideal energy solution to convert the mechanical energy of human motion into electrical energy for the operation of the sweat monitoring system. Triboelectric nanogenerator (TENG) emerging as a new energy harvesting technology, which can efficiently convert mechanical energy into electrical energy based on the coupling effect of triboelectrification and electrostatic induction.[28–30] Owing to the merits of low cost, easy fabrication, high stability, multi-mode operation, and high conversion efficiency, TENG is considered as an ideal energy strategy for next-generation wearable electronics.[31–34] Song et al. reported a self-powered wearable wireless sweat sensing system entirely powered by TENG.[35] The system harvests energy from human motion via TENG to power multiplexed sweat biosensors, which is a milestone work combining TENG with sweat sensor. However, due to the inherent low output power of TENG, it takes up to 4 ≈ 6 min to obtain each set of sensing data. If the sensing period is too

---

Y. Gai, Z. Li
School of Chemistry and Chemical Engineering
Guangxi University
Nanning 530004, China

Y. Gai, E. Wang, M. Liu, Y. Yang, J. Xue, X. Qu, Y. Xi, L. Li, D. Luo, Z. Li
CAS Center for Excellence in Nanoscience
Beijing Key Laboratory of Micro-nano Energy and Sensor
Beijing Institute of Nanoenergy and Nanosystems
Chinese Academy of Sciences
Beijing 100083, China
E-mail: luodan@binn.cas.cn; zli@binn.cas.cn

L. Xie, Y. Bai, Z. Li
Center on Nanoenergy Research
School of Physical Science and Technology
Guangxi University
Nanning 530004, China

J. Xue
School of Nanoscience and Technology
University of Chinese Academy of Sciences
Beijing 100049, China

Z. Li
Institute for Stem Cell and Regeneration
Chinese Academy of Sciences
Beijing 100101, China

The ORCID identification number(s) for the author(s) of this article can be found under https://doi.org/10.1002/smtd.202200653.

DOI: 10.1002/smtd.202200653

long, it is difficult to accurately reflect the changing trend of biomarkers during exercise. Improving the output of the TENG to shorten the sensing periods of the self-powered wireless sweat sensing system is a challenge. TENG has the characteristics of high output voltage and low current, while electromagnetic generator (EMG) has the characteristics of large output current and low voltage, which can be complementary to TENG. Hybridizing TENGs with EMGs exploits their complementarity to effectively improve the output power, which will address the power consumption requirements of the wearable electronics.

Here, we present a self-powered wearable sweat analysis system (SWSAS), which can shorten the acquisition time of sensing data to 1 min. The SWSAS harvests energy from human motion through hybrid nanogenerators, performs selective in situ monitoring of biomarkers (Na^+ and K^+), and wirelessly transmits the sensing data to the user interface via Bluetooth (**Figure 1**a). The SWSAS mainly consists of two hybrid nanogenerator modules (HNGMs), a low-power integrated circuit board, and a replaceable flexible sweat sensor patch. The HNGM, as a self-sustainable power source for SWSAS, is fabricated by hybrid TENG and EMG. Through the spring-mass coupled mechanical design, HNGM can effectively harvest energy from low-frequency, low-acceleration vibrations generated by human motion. The low-power circuit board integrates a power management module, a sensing analog circuit, and a Bluetooth Low Energy (BLE) module for energy management, signal processing, and wireless communication. The flexible sweat sensor patch is entirely laser-engraved, allowing for rapid mass-manufacturing while ensuring wearing comfort. The SWSAS was successfully validated in real-time on-body sweat sensing, indicating its great potential for application in personalized health care. This work provides a promising strategy for advancing self-powered wearable electronics and multifunctional health monitoring platforms.

2. Results and Discussion

Figure 1a depicts a scenario demonstration of wearing the SWSAS on a human arm for self-powered wireless sweat sensing during running. The basic schematic structure of the

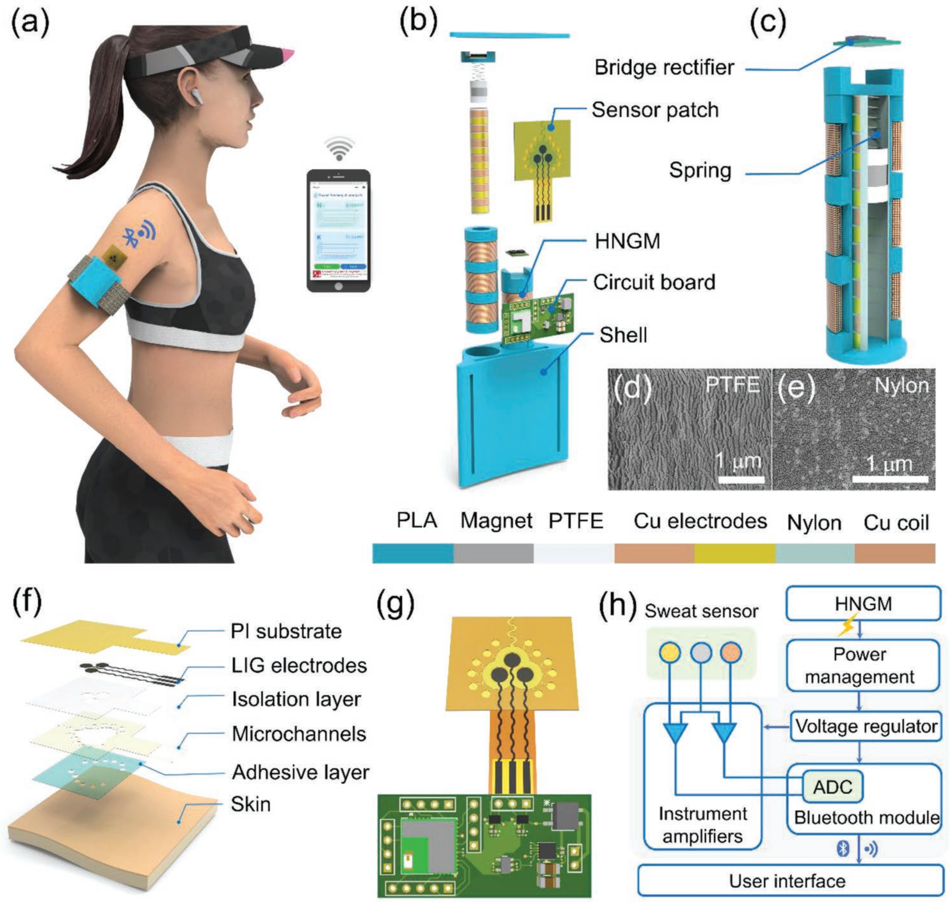

Figure 1. Schematics of the self-powered SWSAS for wireless molecular monitoring. a) Schematic illustration of the SWSAS that efficiently harvesting energy from human motion, performing sweat biosensing, and wirelessly transmitting data to a user mobile interface for real-time health tracking. b) Structure diagram of the SWSAS. c) Structural design of the HNGM. The SEM images of etched d) PTFE and e) nylon film surface. f) Structure diagram of sweat sensor patch. From the bottom layer in contact with the epidermis to the top layer are the adhesive layer, microchannels, insulation layer, LIG electrodes, and PI substrate, respectively. g) Diagram of integrated wearable sweat sensor patch. h) System-level block diagram of the SWSAS showing the energy harvesting, power management, signal transduction, processing, and wireless transmission to the user interface.

SWSAS is illustrated in Figure 1b. The SWSAS consists of two HNGMs for harvesting mechanical energy from human motion, a low-power integrated circuit board for energy management, signal processing, and transmission, a replaceable flexible sweat sensor patch for the detection of biomarkers, and a 3D-printed polylactic acid (PLA) shell. Figure 1c shows the schematic structure of HNGM, which is the self-sustainable power source of SWSAS. The HNGM is fabricated by hybridizing TENG and EMG through spring-mass coupled mechanical design (Figure S1b, Supporting Information). The barrel-shaped support structure of HNGM is 3D printed using PLA, and three grooves are reserved on the outer surface for winding coils. An axially magnetized cylindrical NdFeB magnet (N52, Ø = 8 mm, 10 mm in height) is placed in the barrel-shaped support structure and suspended from the top cap with springs to build the EMG. For TENG, a nylon film was pasted on the surface of the interdigital electrodes fabricated by flexible printed circuit board technology (FPCB) as a positive friction layer. The interdigital electrode with nylon film was axially rolled and attached to the inner wall of the barrel-shaped support structure. Two 3 mm wide PTFE strips are wrapped over the cylindrical magnet at the upper and lower edge (with a gap of 4 mm) as the negative triboelectric layer. Nylon and PTFE films were treated by inductively coupled plasma reactive ion etching to increase the triboelectric charge density.[29,36] Figure 1d,e shows the scanning electron microscope (SEM) images of nanostructures on nylon and PTFE surfaces after etching, respectively. This pair of PTFE strips and interdigitated electrodes with nylon film forms a sliding-mode TENG. As the magnet moves, the PTFE and nylon film slide against each other, generating a triboelectric current between the interdigitated electrodes. At the same time, the movement of the magnet changes the magnetic flux passing through the coils, thereby generating an electromagnetically induced current. The alternating currents generated by TENG and EMG are rectified by two full-wave rectifiers on the top cap and output in parallel, as shown in Figure 1c and Figure S1c, Supporting Information.

The flexible sweat sensor patch is entirely laser-engraved and its preparation process is shown in Figure S8, Supporting Information. The sweat sensor patch contains five layers from the top layer to the bottom layer in contact with epidermis (Figure 1f), including a polyimide (PI) substrate layer, a laser-induced graphene (LIG) electrode layer, an isolation layer (double-sided medical tape), a polyethylene terephthalate (PET) microchannels layer and an adhesive layer (double-sided medical tape). The disposable sensor patch is connected to the printed circuit board (PCB) to perform electrochemical sensing, signal processing, and transmission, as shown in Figure 1g. The PCB is integrated with a power management module, voltage regulator, instrument amplifiers, and the BLE programmed system on a chip (PSoC) module. Schematic diagram of the PCB circuit is shown in Figure S9, Supporting Information. The system-level block diagram of the SWSAS is shown in Figure 1h. HNGMs convert the vibrational mechanical energy generated during human motion into electricity and output it in direct current. The energy management module stores the harvested electricity in two capacitors connected in parallel and releases it logically through a built-in switch. When the voltage of the storage capacitor reaches the threshold value (3.3 V), the electricity will be released, which will power the instrument amplifiers and BLE PSoC module to complete the signal processing and transmission after voltage regulator. When the voltage of the storage capacitors decreases to 2.2 V, the power management module stops the power supply until the storage capacitors are recharged to 3.3 V. The response voltages of chemical sensing are amplified by instrument amplifiers and then read and recorded by the analog-to-digital converters (ADC) integrated into the BLE PSoC module. The acquired sensing data are wirelessly transmitted to a user's mobile interface via BLE for health tracking.

The basic working principle of HNGM can be explained in two parts: TENG and EMG. **Figure 2**a,b,c illustrates the working principle of the TENG. The TENG involved in this work is based on the unique conjugation between triboelectrification and electrostatic induction, and its generation process consists of triboelectric charging and sliding electrostatic induction.[37,38] Under external excitation, the magnet oscillates up and down, causing the PTFE wrapped around the magnet to make contact and slide friction with the nylon film. Due to the difference in triboelectric polarity, the surface of the PTFE film accumulates negative charges while the surface of the nylon film accumulates an equal number of positive charges, which induces equal positive and negative charges on the interdigital electrodes. Next is the sliding electrostatic induction process, which is divided into four steps, as shown in Figure 2b. The initial state is designated when the PTFE film completely overlapped with the electrode A of the interdigital electrode (Figure 2b–i). In this state, the two consecutive interdigitated electrodes are in an electrostatic equilibrium state, and there is no charge flow. When the magnet moves downward, the PTFE gradually moves from electrode A to electrode B. Under electrostatic induction, electrons flow from electrode B to electrode A through the external load (Figure 2b–ii). When the PTFE film completely overlaps electrode B, electrons are completely transferred from electrode B to electrode A, resulting another charge equilibrium state (Figure 2b–iii). Similarly, as the magnet moves upward, electrons flow back from electrode A to electrode B, resulting a reverse current (Figure 2b–iv). Therefore, as the magnet periodically oscillates up and down, the electrons will periodically transfer between the interdigitated electrodes, resulting a continuous AC output. Furthermore, according to the actual size of the TENG, a finite element simulation of the potential distribution between PTFE and nylon in each step was performed by using COMSOL Multiphysics software (Figure 2c), so as to better understand and analyze the working principle of TENG.

Figure 2d,e,f illustrates the working principle of the EMG. The EMG is based on the principle of electromagnetic induction, which generates AC due to the periodic variation of magnetic flux in the coils.[39] In the initial state, the magnet is stationary relative to the upper coil, and there is no current in the coil (Figure 2e–i). As the magnet moves downward, the magnetic flux crossing the coil changes, creating an induced current until it coincides with the lower coil (Figure 2e-ii–iii). As the magnet moves upward, the magnetic flux crossing the coils is in the opposite direction, resulting a reverse induced current (Figure 2e–iv). Similarly, as the magnet periodically oscillates up and down, a continuous induced current will be generated

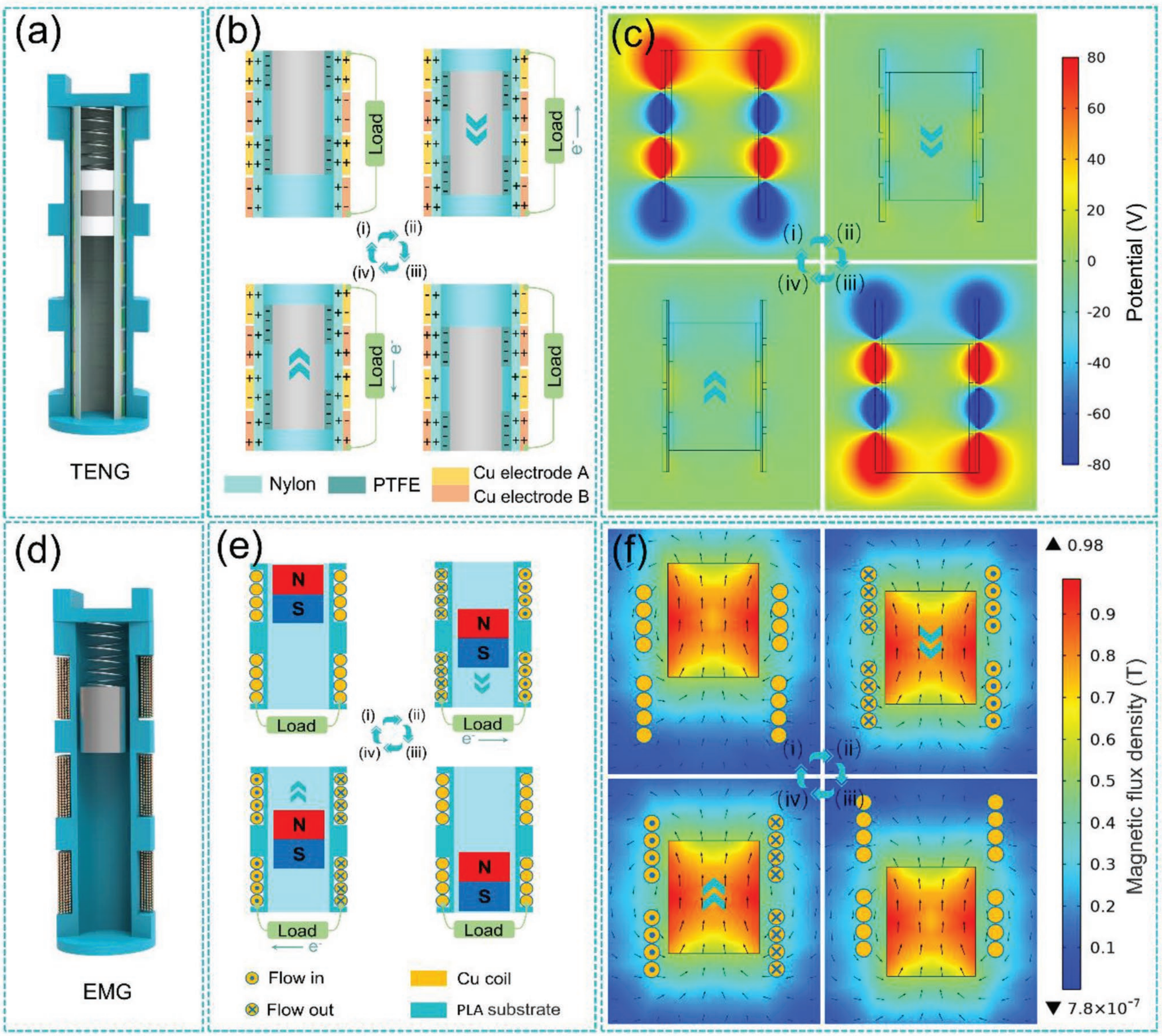

Figure 2. The working mechanism of the HNGM. a) Structural design of the TENG. b) Schematic illustration of the working mechanism of TENG. c) Finite element analysis simulation of TENG showing electric potential distribution. d) Structural design of the HNGM. e) Schematic illustration of the working mechanism of EMG. f) Finite element analysis simulation of EMG showing magnetic flux distribution.

in the coils. The magnetic flux density of magnet is also studied through finite element simulation, as shown in Figure 2f.

The output performance of TENG, EMG, and HNGM was investigated by using linear motors to provide external excitation. Under the vibration excitation frequency of 5 Hz, the open-circuit voltage (V_{OC}) and short-circuit current (I_{SC}) of TENG are about 60 V and 4 μA, as shown in **Figure 3**a,b, respectively. Meanwhile, the V_{OC} and I_{SC} of EMG under the same excitation conditions are about 14 V and 14 mA, as shown in Figure 3d,e. Compared with TENG, the EMG generates a higher I_{SC} and a lower V_{OC}. The V_{OC} and I_{SC} of both TENG and EMG after rectification are shown in Figure S2, Supporting Information. Figure 3c,f shows the output power performance of TENG and EMG with various load resistance. The output voltage of TENG and EMG increases with increasing load resistance, while the output current decreases. The peak power of both TENG and EMG increases with the increase of the load resistance, and decreases with the further increase of the load resistance after reaching the maximum value. The TENG reaches a maximum output power of 81 μW at 10.5 MΩ, and the EMG reaches a maximum output power of 43.5 mW at 1000 Ω. Figure S4, Supporting Information compared the output performance and charging performance of TENG and EMG at low frequency. The results show that TENG has more advantages than EMG in low-frequency mechanical energy harvesting.

Figure 3g,h shows that the V_{OC} and I_{SC} of HNGM are about 60 V and 15 mA, respectively. It exhibits the characteristics of high voltage for TENG and high current for EMG. Figure 3j shows the voltage curves of a 330 μF capacitor charged by TENG, EMG, and HNGM. Compared with TENG and EMG,

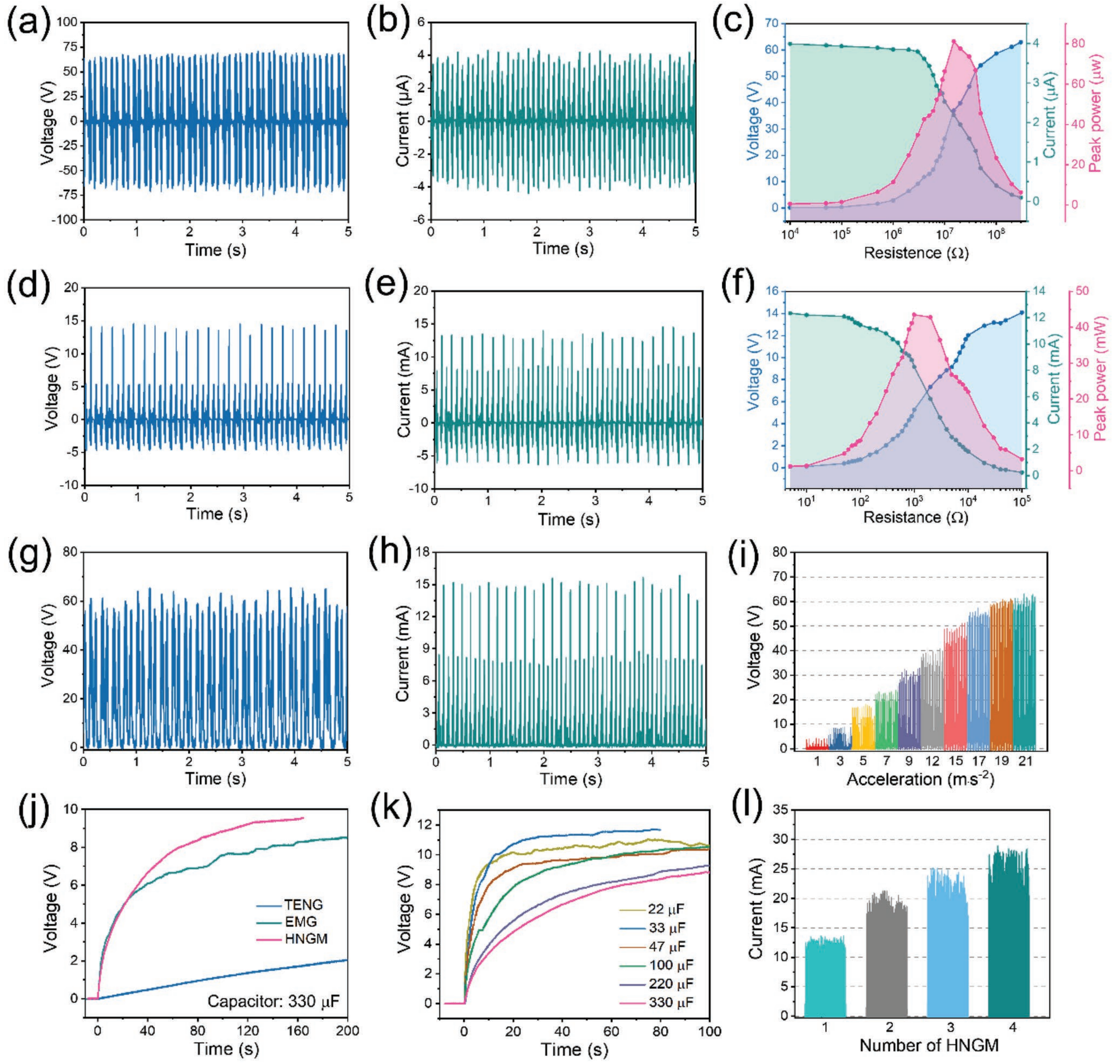

Figure 3. The output performance of the TENG, EMG, and HNGM. The a) V_{OC} and b) I_{SC} of TENG. c) Resistance dependence of the V_{OC}, I_{SC}, and peak power of TENG. The d) V_{OC} and e) I_{SC} of EMG. f) Resistance dependence of the V_{OC}, I_{SC}, and peak power of EMG. The g) V_{OC} and h) I_{SC} of HNGM. i) The V_{OC} of HNGM at different acceleration. j) Charging curve of a 330 μF capacitor charged by TENG, EMG, and HNGM, respectively. k) Charging voltage on various capacitances for the HNGM. l) The current of different numbers of HNGMs in parallel.

HNGM has better-charging performance. As can be seen from the charging curve of HNGM, EMG with large output power plays a dominant role in the initial charging stage. After the capacitor is charged to 5.5 V, the effect of TENG is gradually obvious. The characteristics of high output voltage for TENG can help HNGM break the maximum voltage stored in the capacitor limited by EMG. Meanwhile, the high output power of EMG can solve the power shortage problem of TENG when driving high-power electronic loads. Figure 3k shows the voltage curves of HNGM charging different commercial capacitors. The charging speeds of HNGM are all fast in the initial stage of charging the capacitors and then trend to smooth. The larger the capacity of the capacitor, the longer the charging time. The charging performance of TENG and EMG was also evaluated, as shown in Figure S2c,f, Supporting Information. Due to the unique mechanical design of the spring-mass coupling, acceleration plays a decisive role in the performance output of the HNGM. The V_{OC} of HNGM increases from 4 to 62 V with acceleration increases from 1 to 21 m s^{-2}. When the acceleration reaches 19 m·s^{-2}, the magnet will go beyond the restraint of the spring and hit the shell directly.

In our daily life, the motion of the human body is random and anisotropic. Therefore, the angle between HNGM and the direction of motion is taken as the research object to study the output performance of HNGM under different angles. The results show that HNGM can obtain motion energy from different directions (Figure S6, Supporting Information). The HNGM can be stacked as a unit of the energy harvester. Four HNGMs in parallel can output a current of 27 mA, as shown in Figure 3l. The HNGM has excellent energy harvesting capabilities, which can light up multiple LED lights and charge the smart bracelet, as shown in Figure S2g,h,i and Movie S1 and S2, Supporting Information.

Figure 4a depicts the schematic of electrochemical sensor for sweat biomarkers analysis. Graphene is widely used to construct electrochemical sensors to detect low levels of electroactive analytes due to its ultra-large specific surface area, fast electron mobility, and high current density.[16,40–42] Here, graphene electrodes were prepared on PI films by using laser engraving. The SEM images of LIG are shown in Figure 4c,d. The LIG presents a foam-like structure of randomly stacked ultra-thin nanosheets. Raman spectroscopy and X-ray diffraction (XRD) of LIG were also performed, as shown in Figure S7e,f, Supporting Information. The sharp 2D band along with the G band in Raman spectra and the clearly (002) XRD peak indicate the successful preparation of graphene materials.[43–45]

The ion-selective electrodes (ISEs) were constructed by modifying LIG electrodes with highly specific chemistries. For Na^+ ISE, a poly(3,4-ethylenedioxythiophene) polystyrene sulfonate (PEDOT:PSS) layer and a Na^+ selective membrane containing Na^+ ionophore X were successively modified on the LIG electrode. Similarly, a PEDOT:PSS layer and a K^+ selective membrane containing valinomycin were successively modified on the LIG electrode to prepare K^+ ISE. The PEDOT:PSS layer acts as an ion-electron transducer in the ISEs that can minimize the potential drift of the biosensor.[13,35,46] An Ag/AgCl electrode serves as the common reference electrode for Na^+ and K^+ ISE. The reference electrode is coated with polyvinyl butyral (PVB) to maintain the reference voltage in sweat with different ionic strengths, reducing the interaction between the ion-selective sensors.[21] The laser-patterned microfluidic channel can enhance the sweat sampling process and improve the temporal resolution of sweat sensing. Under the action of the capillary force of the microfluidic channel, the sweat is collected into the sensing chamber from the reserved inlets, and discharged from the outlet after sensing, as shown in Figure 4b. The flexible sweat sensing patch can be closely attached to the skin surface for in-situ sensing, which can effectively avoid the evaporation and the contamination of sweat during exercise, and maintain the stability of the sweat sensing environment.

The electrochemical responses of Na^+ and K^+ sensors were characterized in NaCl solution of 5–160 mM and KCl solution of 0.625–40 mM, respectively. As depicted in Figure 4e,h, the $Na^{+,}$ and K^+ sensors show near-Nernstian sensitivities of 67.43 and 30.42 mV per decade of ion concentration, respectively. The five sweat sensors manufactured in different batches have similar potential responses with low variation in sensitivity, indicating the good reproducibility (Figure 4f,i). The specificity of Na^+ and K^+ sensors was verified by adding various interfering ions to NaCl and KCl solutions, respectively. As depicted in Figure 4j,h, the electrochemical response curves of Na^+ and K^+ sensors did not change noticeably with the addition of interfering ions, indicating excellent specificity. Also, the Na^+ and K^+ sensors shown long-term sensing stability during the test in three concentrations of solution for 3 h (Figure 4l). The potential response of the Na^+ and K^+ sensors remained stable after repeated bending for 200 times at 60°, demonstrating reliable mechanical stability of the sweat sensor patch (Figure 4k). In addition, the effect of temperature on the sweat sensor was also evaluated. As can be seen from Figure S11, Supporting Information, the potential responses of the Na^+ and K^+ sensors hardly change with the increase in temperature, indicating that the $Na^{+,}$ and K^+ sensors are not affected by temperature.

To evaluate the on-body energy harvesting capability of the HNGM, a HNGM was tied to a volunteer's arm to test its output voltage and current under different activities such as walking, running, and jumping (Move S3, Supporting Information). As shown in **Figure 5**a, the output performance of HNGM increases gradually with the increase of the exercise intensity. In the jumping state, the output voltage and current of HNGM reached 35 V and 3 mA, respectively, indicating the excellent on-body energy harvesting capability.

Figure 5b,c shows the functional logic diagram of the SWSAS. The AC output generated by the TENG and EMG was converted to DC output by two low-loss full-wave rectifier bridges, which are then output in parallel. The power management integrated circuit (PMIC) stores the energy harvested by the HNGM in storage capacitors, and releases the energy on demand through logic control for the operation of the sensing system to minimize the waste of energy. When the voltage of the storage capacitor (V_{STORE}) reaches 3.3 V, the PMIC releases electrical energy to power the sensing circuit and the BLE PSoC module. When the V_{STORE} drops to 2.2 V, the PMIC cuts off the electrical energy release until the storage capacitor is recharged to 3.3 V. The electrical energy released by the PMIC is adjusted to 2.2 V by a voltage regulator to provide a stable voltage (V_{DD}) to the sensing circuit and BLE PSoC module. After the BLE PSoC module starts, the central processing unit wakes up the instrument amplifiers. The ADC embedded in the BLE PSoC module processes the potential signal obtained from the instrumentation amplifiers. After the ADC completes processing, the module turns off the instrumentation amplifiers and wirelessly transmits the processing result to the user interface via BLE. The whole process of sensor data processing and transmission is about 12 milliseconds.

The fully integrated SWSAS can be easily worn on the human body, such as the forearm, upper arm, calf, and thigh, to convert the vibration energy generated by human movement into electrical energy, and drive the sweat sensor for wireless sweat sensing (Figure S16, Supporting Information). Figure 5d shows the volunteer wearing the SWASA while running. The sweat patch is attached to the skin with a laser-patterned double-sided medical tape (Figure 5e). Figure 5g shows the charging and discharging curve of the storage capacitor on the PCB during the running exercise of the volunteer. When the voltage of the storage capacitor reaches 3.3 V, the energy management module releases power to the instrument amplifier and BLE PSoC module for a single measurement and transmission. The

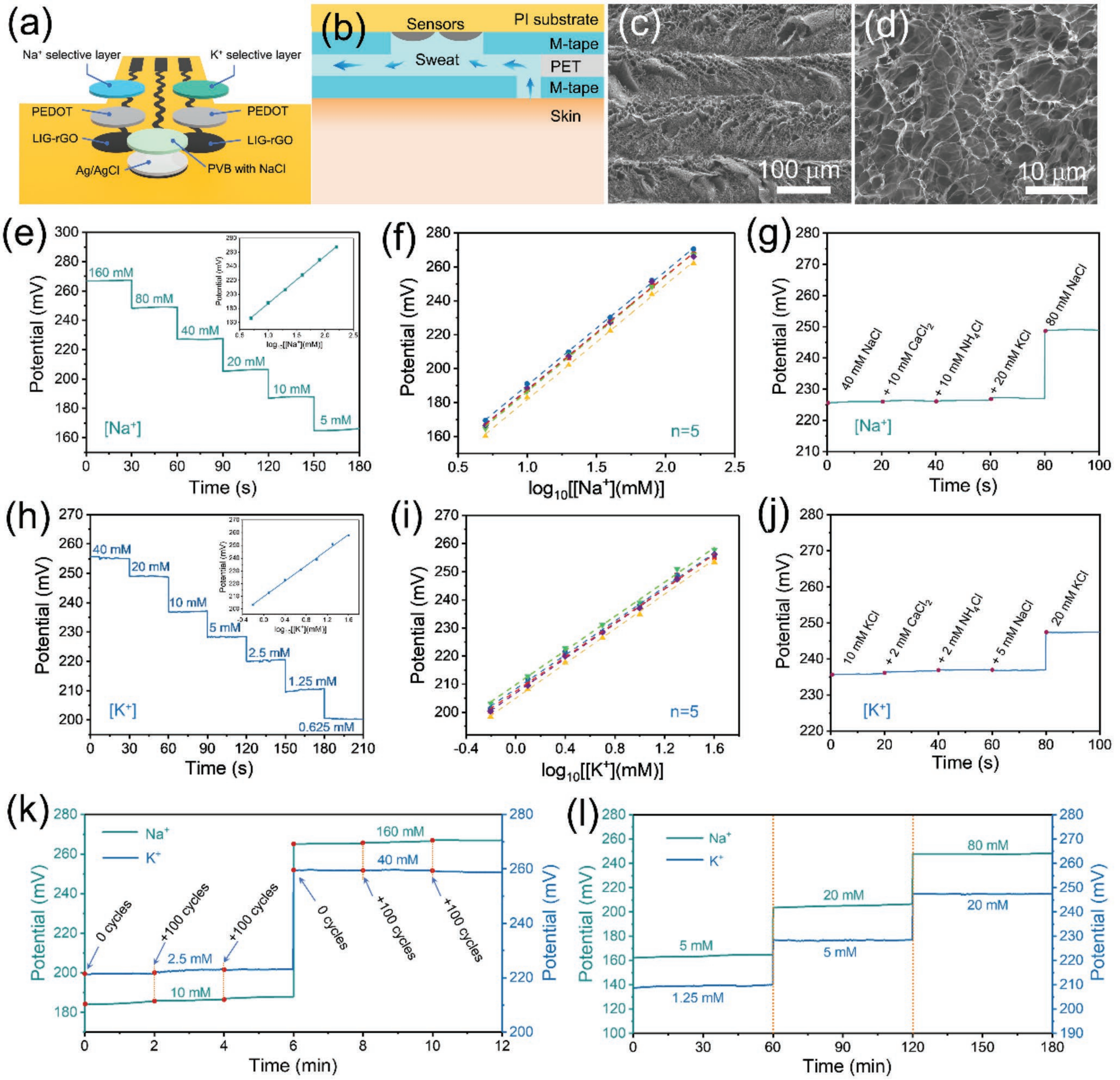

Figure 4. Schematics and characterization of the microfluidic sweat sensor patch. a) Schematic illustration of the multiplex electrochemical sensor assemblies. b) Layout of microfluidic sweat sensor patch. M-tape: medical tape. c,d) SEM images of the LIG. e) Open-circuit potential response of Na^+ sensor in NaCl solution. f) Consistency valuation of Na^+ sensors. g) Selective evaluation of Na^+ sensors. h) Open-circuit potential response of K^+ sensor in KCl solution. i) Consistency valuation of K^+ sensors. j) Selective evaluation of K^+ sensors. k) Mechanical reliability of the sweat sensor patch with 200 cycles of bending. l) Stability verification of the sensor for continuous test 3 h.

charging/discharging period of the storage capacitor ranges from 33 to 60 s, which means that on average one measurement data can be obtained in one minute. The acquired data is wirelessly sent to the user interface by BLE (Figure 5f). The user interface included the real-time data and plots of Na^+ and K^+ concentrations.

The volunteer was asked to run continuously outdoors for 35 minutes with an average speed of about 7.2 km h^{-1} to perform on-body validation for the SWSAS. Figure 5h shows the concentration plots of Na^+ and K^+ during the whole exercising process. After ≈9 min of running, the first pair of signal data was obtained. Overall, with the extension of exercise time, the concentration of Na^+ shown a rising trend from 36.81 to 41.21 mM, while the concentration of K^+ shown a decreasing trend from 11.86 to 7.86 mM, which are similar trends to the previous research results.[13,21,46] The Na^+ and K^+ concentrations detected by the SWSAS were within the normal physiologically relevant concentration range, indicating that the system has

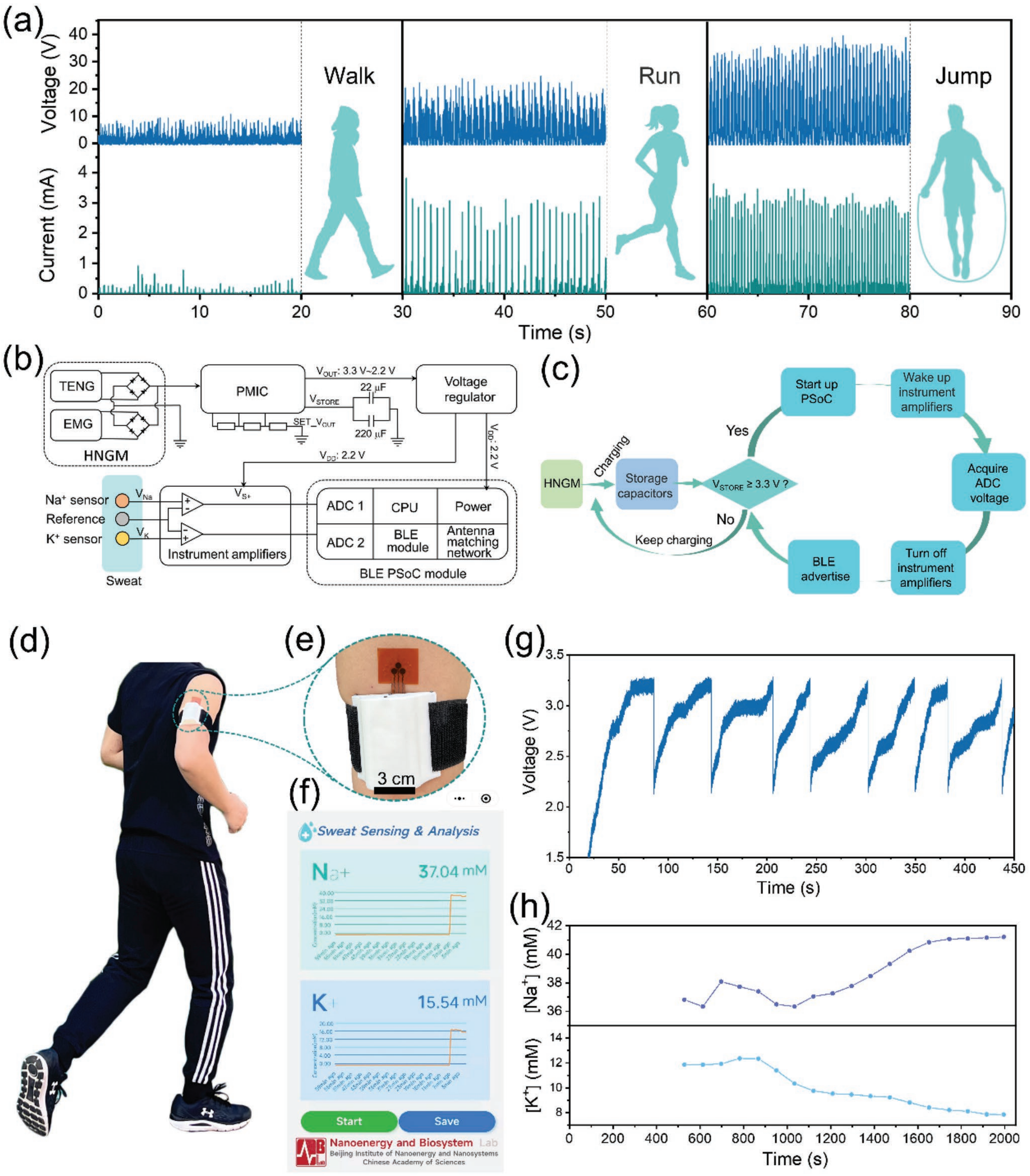

Figure 5. Real-time on-body sweat sensing and data transmission powered by HNGM. a) Output performance of energy harvesting devices during walking, running, and jumping. b) Module diagram of the SWSAS. c) Operation flow of the SWSAS. d) A photograph of an individual with the SWSAS strapped to the arm during running. The SWSAS wirelessly senses of Na^+ and K^+ in sweat via Bluetooth and records the data to a mobile phone. e) A photograph of SWSAS strapped to the arm. f) Mobile phone interface of sweat sensing and analysis developed based on WeChat applet. g) Real-time potential of the capacitor charged by an HNGM. h) The real-time concentration of Na^+ and K^+ in sweat during running by using SWSAS.

good performance in real-time on-body sweat sensing.[10,47,48] In addition, the volunteer was also asked to jump rope indoors to demonstrate the operation of SWASAS (Movie S4, Supporting Information).

3. Conclusion

In summary, this work presents a battery-free, self-powered wearable sweat analysis system that is completely powered by human motions. Based on the coupled EMG and TENG design, HNGM can effectively convert the mechanical energy of human motions into electricity to drive the sweat analysis system. Highly integrated low-power circuit board enables efficient management of harvested energy and minimize power consumption for information processing and transmission. The entirely laser-engraved flexible sweat sensor patch can conform to the skin for automatic collection and analysis of sweat. As a proof of concept, real-time on-body sweat analysis further carried out with a volunteer in running. The system successfully realized the wireless monitoring of biomarkers in sweat and recorded the concentration fluctuations of Na^+ and K^+ while the volunteer was running, indicating its potential application in wireless personalized health monitoring and exercise optimization. This work demonstrates an important attempt to construct battery-free, fully self-powered wearable electronics. With proper optimization, we believe that this technology will be able to serve as a universal platform for future self-powered electronics.

4. Experimental Section

Materials and Reagents: Polytetrafluoroethylene (PTFE, 75 µm), polyimide (PI, 100 µm), and nylon 6/6 (75 µm) film were purchased from DuPont. Polyethylene terephthalate (PET, 100 µm) film was purchased from McMaster–Carr. Double-sided medical tapes were purchased from 3 M. 3,4-Ethylenedioxythiophene (EDOT), sodium polystyrene sulfonate (NaPSS), sodium ionophore X, valinomycin, sodium tetrakis [3,5-bis(trifluoromethyl)phenyl] borate (Na-TFPB), sodium tetraphenylboron (NaTPB), bis(2-ethylehexyl) sebacate (DOS) and block polymer PEO-PPO-PEO (F127) were purchased from Sigma–Aldrich. Sodium thiosulfate pentahydrate ($Na_2S_2O_3$), sodium bisulfite ($NaHSO_3$), silver nitrate ($AgNO_3$), iron (III) chloride ($FeCl_3$), calcium chloride dihydrate ($CaCl_2 \cdot 2H_2O$), Sodium chloride (NaCl), Potassium chloride (KCl), ammonium chloride (NH_4Cl) and multiwall carbon nanotubes (MWCNTs), were purchased from Macklin. Polyvinyl Butyral (PVB), polyvinyl chloride (PVC), methanol, ethanol, acetone, tetrahydrofuran (THF), aniline, cyclohexanone, and were purchased from Aladdin. All the above-mentioned chemicals were used as received.

Fabrication of HNGM: Both the shell and the barrel-shaped support structure used to wrap the coils were fabricated by a 3D printer (Raize 3D) using PLA. The barrel-shaped support ($Ø_{outer}$ = 16 mm, $Ø_{inner}$ = 9 mm) structure had three annular slots (10 mm in width, 5 mm in depth) for winding copper coils. The copper coils were made of copper wire with a diameter of 0.08 mm. The interdigital electrodes of TENG were fabricated by flexible FPCB. A nylon film was covered on the interdigital electrodes as the positive triboelectric layer. The interdigital electrode with nylon film was axially rolled and attached to the inner wall of the barrel-shaped support structure. An axially magnetized cylindrical magnet (N52, Ø = 8 mm, 10 mm in height) was placed in the barrel-shaped support structure. The PTFE film was attached to the upper and lower edges of the magnet as the negative triboelectric layer. The nylon and PTFE films were pretreated inductively coupled plasma reactive ion etching. A spring (Ø = 8 mm, 10 mm in height) made of 0.2 mm steel wire was attached at one end to the magnet and at the other end to a top cap. The top cap (Ø = 16 mm, 5 mm in height) had a groove for installing two rectifier bridges.

Fabrication of Sweat Sensor Patch: The patterned LIG electrodes were produced by etching a PI film with a 75 W CO_2 laser cutter in raster mode. The optimized power was 10% and the speed was 100 mm s^{-1}. The isolation layer, microchannels layer, and adhesive layer were created by cutting corresponding material with laser cutter in vector mode. The optimized power was 15% and the speed was 100 mm s^{-1}. The microchannel layer was cut from PET film. Both isolation layer and adhesive layer were cut from waterproof double-sided medical tape. The LIG electrodes were deposited and modified with different functional materials to form Ag/AgCl reference electrode, Na^+ and K^+ ISEs, respectively. Finally, the LIG electrode layer, isolation layer, microchannel layer, and adhesive layer were laminated together in sequence to form a sweat sensor patch.

Modification of LIG Electrodes: Electrodeposition and electrochemical polymerization were performed on an electrochemical workstation (CHI660E). The LIG electrodes were modified by referring to the methods in the reported literature.[13,14,16,35,46] The Na^+ and K^+ ISEs share an Ag/AgCl reference electrode. To prepare the reference electrode, Ag onto the LIG electrode using constant voltage electrodeposition is deposited (–0.25 V for 600 s) in a deposition solution containing 0.25 M $AgNO_3$, 0.75 M $Na_2S_2O_3$, and 0.43 M $NaHSO_3$. Then, 0.1 M $FeCl_3$ solution was dropped onto the Ag surface for 60 s to form Ag/AgCl. After that, the PVB reference solution was prepared, and 10 µl of the PVB reference solution was drop-coated onto the Ag/AgCl electrode. The PVB reference solution was prepared by dissolving 79.1 mg PVB, 50 mg NaCl, 1 mg F127, and 0.2 mg MWCNT in 1 ml methanol.

The Na^+ and K^+ ISEs consist of PEDOT layer and ion-selective membrane. The PEDOT layer was used as an ion-electron transducer, which can minimize the potential drift of the ISEs. To prepare PEDOT layer, an electrodeposition solution containing 0.01 M EDOT and 0.1 M NaPSS was used to deposit PEDOT:PSS on the LIG electrode by galvanostatic electrochemical polymerization under the current of 14 µA for 600 s. The Na^+ selective solution was prepared by dissolving the mixture (200 mg) of Na+ ionophore X (1%, w/w), Na-TFPB (0.55%, w/w), DOS (65.45%, w/w) and PVC (33%, w/w) into THF (1320 µl). Then, the Na^+ selective membrane was prepared by drop-casting 10 µl of Na^+ selective solution onto the PEDOT layer and dried overnight. Similarly, the K^+ selective solution was prepared by dissolving the mixture (200 mg) of valinomycin (2%, w/w), NaTPB (0.5%, w/w), DOS (64.7%, w/w) and PVC (32.8%, w/w) into cyclohexanone (700 µl). Then, the K^+ selective membrane was then prepared by drop-casting 10 µl of K^+ selective solution onto the PEDOT layer and dried overnight. The solutions above were sealed and stored at 4 °C when not in use.

Characterization of HNGM and Materials: The V_{OC} and I_{SC} were measured by an electrometer (Keithley 6517) with an oscilloscope (Teledyne LeCroy HDO 8108A). A linear motor (LinMot E1100) was used to provide periodic motion for testing output performance at different accelerations and long-term operation. The SEM images of PTFE and nylon film were taken by field emission scanning electron microscope (SEM, Hitachi SU8020). The crystal and elementary composition of the LIG were analyzed by X-ray diffractometer (PANalytical X'Pert) with Cu Kα radiation, and Raman spectra (LabRAM HR Evolution, Horiba).

Characterization of Sweat Sensor: To minimize the potential drift of the ISEs and obtain the best sensing performance, the sweat sensors were placed in a solution containing 0.1 M NaCl and 0.1 M KCl for 1 h before measurements. NaCl solution from 5 mM to 160 mM, and KCl solution from 0.625 to 40 mM were used to characterize the electrochemical responses of Na^+ and K^+ ISEs, respectively. Five sweat sensors fabricated in different batches were characterized to investigate the reproducibility. To verify the selectivity of Na^+ ISE, 10 mM $CaCl_2$, 10 mM NH_4Cl, and 20 mM KCl were successively added to the 40 mM NaCl solution. While the selectivity of K^+ ISE was characterized by the successive addition of 2 mM $CaCl_2$, 2 mM NH_4Cl, and 5 mM NaCl into a 10 mM KCl solution. The long-term stability of the sweat sensors was tested continuously for 3 h in three concentrations of solution. The mechanical reliability of sweat sensor patches was investigated by repeatedly bending them for 200 cycles. The electrochemical responses of the sweat sensor patches were measured every 100 cycles in two concentrations of solution.

On-Body Evaluation of the SWSAS: The on-body sweat detection experiment was performed by a healthy male volunteer, who was also a co-author of the manuscript. The volunteer was informed and signed the consent form before participating in the experiment. All experiments were approved by the Committee on Ethics of Beijing Institute of Nanoenergy and Nanosystems (A-2020009).

The fully integrated SWSAS was worn on the volunteer's arm using elastic straps. The skin where the sensor patch was attached was wiped with alcohol swabs in advance. To evaluate the SWSAS on-body, the volunteer was asked to run continuously outdoors for 35 min, with an average speed of ≈7.2 km h^{-1}. In addition, the volunteer was also asked to perform a rope skipping test indoors, and a video was filmed to demonstrate the operation of SWASAS.

Supporting Information

Supporting Information is available from the Wiley Online Library or from the author.

Acknowledgements

This study was supported by the National Natural Science Foundation of China (61875015, T2125003), the Strategic Priority Research Program of the Chinese Academy of Sciences (XDA16021101), and the Beijing Natural Science Foundation (JQ20038, L212010).

Conflict of Interest

The authors declare no conflict of interest.

Author Contributions

Y.G. and Z.L. conceived the project. Y.G. designed the experiment and fabricated the device. M.L. wrote the WeChat applet. Y.G., L.X., X.Q. accomplished the PCB. Y.G., E.W., Y.B., Y.Y., Y.X., and L.L. carried out the electrical characterization and the material characterization. J.X. performed the finite element simulation. Y.G. D.L and Z.L. prepared the manuscript. All authors discussed and reviewed the manuscript.

Data Availability Statement

The data that support the findings of this study are available from the corresponding author upon reasonable request.

Keywords

personalized health care, self-powered systems, sweat sensors, wearable electronics, wireless communication

Received: May 19, 2022
Revised: August 23, 2022

---

[1] M. Tan, Y. Xu, Z. Gao, T. Yuan, Q. Liu, R. Yang, B. Zhang, L. Peng, *Adv. Mater.* **2022**, *34*, 2108491.
[2] H. Sheng, X. Zhang, J. Liang, M. Shao, E. Xie, C. Yu, W. Lan, *Adv. Healthcare Mater.* **2021**, *10*, 2100199.
[3] Y. Yu, H. Y. Y. Nyein, W. Gao, A. Javey, *Adv. Mater.* **2020**, *32*, 1902083.
[4] Y. Lin, M. Bariya, A. Javey, *Adv. Funct. Mater.* **2021**, *31*, 2008087.
[5] Y. Ma, Y. Zhang, S. Cai, Z. Han, X. Liu, F. Wang, Y. Cao, Z. Wang, H. Li, Y. Chen, X. Feng, *Adv. Mater.* **2020**, *32*, 1902062.
[6] Y. Liu, M. Pharr, G. A. Salvatore, *ACS Nano* **2017**, *11*, 9614.
[7] M. Bariya, H. Y. Y. Nyein, A. Javey, *Nat. Electron.* **2018**, *1*, 160.
[8] J. Choi, R. Ghaffari, L. B. Baker, J. A. Rogers, *Sci. Adv.* **2018**, *4*, eaar3921.
[9] Y. Fang, L. Meng, A. Prominski, E. N. Schaumann, M. Seebald, B. Tian, *Chem. Soc. Rev.* **2020**, *49*, 7978.
[10] E. J. M., J. R. H. Moonen, E. Peri, E. Pelssers, M. Mischi, J. M. J. den Toonder, *View* **2020**, *1*, 20200077.
[11] H. C. Ates, A. Brunauer, F. von Stetten, G. A. Urban, F. Guder, A. Merkoci, S. M. Fruh, C. Dincer, *Adv. Funct. Mater.* **2021**, *31*, 2010388.
[12] Y. Song, D. Mukasa, H. Zhang, W. Gao, *Acc. Mater. Res.* **2021**, *2*, 184.
[13] W. Gao, S. Emaminejad, H. Y. Y. Nyein, S. Challa, K. Chen, A. Peck, H. M. Fahad, H. Ota, H. Shiraki, D. Kiriya, D. H. Lien, G. A. Brooks, R. W. Davis, A. Javey, *Nature* **2016**, *529*, 509.
[14] W. He, C. Wang, H. Wang, M. Jian, W. Lu, X. Liang, X. Zhang, F. Yang, Y. Zhang, *Sci. Adv.* **2019**, *5*, eaax0649.
[15] H. Hojaiji, Y. Zhao, M. C. Gong, M. Mallajosyula, J. Tan, H. Lin, A. M. Hojaiji, S. Lin, C. Milla, A. M. Madni, S. Emaminejad, *Lab Chip* **2020**, *20*, 4582.
[16] Y. Yang, Y. Song, X. Bo, J. Min, O. S. Pak, L. Zhu, M. Wang, J. Tu, A. Kogan, H. Zhang, T. K. Hsiai, Z. Li, W. Gao, *Nat. Biotechnol.* **2020**, *38*, 217.
[17] G. Xu, C. Cheng, W. Yuan, Z. Y. Liu, L. H. Zhu, X. T. Li, Y. L. Lu, Z. T. Chen, J. L. Liu, Z. Cui, J. J. Liu, H. Men, Q. J. Liu, *Sens. Actuators, B* **2019**, *297*, 126743.
[18] L. B. Baker, J. B. Model, K. A. Barnes, M. L. Anderson, S. P. Lee, K. A. Lee, S. D. Brown, A. J. Reimel, T. J. Roberts, R. P. Nuccio, J. L. Bonsignore, C. T. Ungaro, J. M. Carter, W. Li, M. S. Seib, J. T. Reeder, A. J. Aranyosi, J. A. Rogers, R. Ghaffari, *Sci. Adv.* **2020**, *6*, eabe3929.
[19] M. Parrilla, K. De Wael, *Adv. Funct. Mater.* **2021**, *31*, 2107042.
[20] L. Manjakkal, L. Yin, A. Nathan, J. Wang, R. Dahiya, *Adv. Mater.* **2021**, *33*, 2100899.
[21] G. Xu, C. Cheng, Z. Y. Liu, W. Yuan, X. Z. Wu, Y. L. Lu, S. S. Low, J. L. Liu, L. H. Zhu, D. Z. Ji, S. Li, Z. T. Chen, L. S. Wang, Q. G. Yang, Z. Cui, Q. J. Liu, *Adv. Mater. Technol.* **2019**, *4*, 1800658.
[22] B. Lee, H. Cho, K. T. Park, J. S. Kim, M. Park, H. Kim, Y. Hong, S. Chung, *Nat. Commun.* **2020**, *11*, 5948.
[23] H. Wu, Y. Zhang, A. L. Kjoniksen, X. Zhou, X. Zhou, *Adv. Funct. Mater.* **2021**, *31*, 2103976.
[24] Y. Su, L. Lu, M. Zhou, *ACS Appl. Mater. Interfaces* **2022**, *14*, 8664.
[25] M. Hatamvand, E. Kamrani, M. Lira-Cantu, M. Madsen, B. R. Patil, P. Vivo, M. S. Mehmood, A. Numan, I. Ahmed, Y. Q. Zhan, *Nano Energy* **2020**, *71*, 104609.
[26] Z. Wen, M. H. Yeh, H. Guo, J. Wang, Y. Zi, W. Xu, J. Deng, L. Zhu, X. Wang, C. Hu, L. Zhu, X. Sun, Z. L. Wang, *Sci. Adv.* **2016**, *2*, 1600097.
[27] Y. Liu, X. Huang, J. Zhou, C. Yiu, Z. Song, W. Huang, S. K. Nejad, H. Li, T. H. Wong, K. Yao, L. Zhao, W. Yoo, W. Park, J. Li, Y. Huang, H. R. Lam, E. Song, X. Guo, Y. Wang, Z. Dai, L. Chang, W. Li, Z. Xie, X. Yu, *Adv. Sci.* **2022**, *9*, 2104635.
[28] Y. Cao, Y. Yang, X. Qu, B. Shi, L. Xu, J. Xue, C. Wang, Y. Bai, Y. Gai, D. Luo, Z. Li, *Small Methods* **2022**, *6*, 2101529.
[29] Y. Gai, Y. Bai, Y. Cao, E. Wang, J. Xue, X. Qu, Z. Liu, D. Luo, Z. Li, *Small* **2022**, *18*, 2108091.
[30] Y. Bai, S. Chen, H. Wang, E. Wang, X. Kong, Y. Gai, X. Qu, Q. Li, S. Xue, P. Guo, R. Wang, H. Feng, Z. Li, *Nano Energy* **2022**, *95*, 106992.

[31] Y. Zhou, M. Shen, X. Cui, Y. Shao, L. Li, Y. Zhang, *Nano Energy* **2021**, *84*, 105887.
[32] R. Zhang, M. Hummelgard, J. Ortegren, M. Olsen, H. Andersson, Y. Yang, H. Zheng, H. Olin, *Nano Energy* **2021**, *86*, 106041.
[33] C. Xu, Y. Song, M. Han, H. Zhang, *Microsyst. Nanoeng.* **2021**, *7*, 25.
[34] J. Zhu, M. Zhu, Q. Shi, F. Wen, L. Liu, B. Dong, A. Haroun, Y. Yang, P. Vachon, X. Guo, T. He, C. Lee, *EcoMat.* **2020**, *2*, e12058.
[35] Y. Song, J. Min, Y. Yu, H. Wang, Y. Yang, H. Zhang, W. Gao, *Sci. Adv.* **2020**, *6*, eaay9842.
[36] P. Tan, Q. Zheng, Y. Zou, B. Shi, D. Jiang, X. Qu, H. Ouyang, C. Zhao, Y. Cao, Y. Fan, Z. Wang, Z. Li, *Adv. Energy Mater.* **2019**, *9*, 1901875.
[37] F. Zheng, Y. Sun, X. Wei, J. Chen, Z. Yuan, X. Jin, L. Tao, Z. Wu, *Nano Energy* **2021**, *90*, 106631.
[38] Z. Yuan, C. Wang, J. Xi, X. Han, J. Li, S. Han, W. Gao, C. Pan, *ACS Energy Lett.* **2021**, *6*, 2809.
[39] B. Zhang, S. Zhang, W. Li, Q. Gao, D. Zhao, Z. L. Wang, T. Cheng, *ACS Nano* **2021**, *15*, 20278.
[40] H. Lee, T. K. Choi, Y. B. Lee, H. R. Cho, R. Ghaffari, L. Wang, H. J. Choi, T. D. Chung, N. Lu, T. Hyeon, S. H. Choi, D. H. Kim, *Nat. Nanotechnol.* **2016**, *11*, 566.
[41] B. Chen, Z. T. Johnson, D. Sanborn, R. G. Hjort, N. T. Garland, R. R. A. Soares, B. Van Belle, N. Jared, J. Li, D. Jing, E. A. Smith, C. L. Gomes, J. C. Claussen, *ACS Nano* **2022**, *16*, 15.
[42] F. M. Vivaldi, A. Dallinger, A. Bonini, N. Poma, L. Sembranti, D. Biagini, P. Salvo, F. Greco, F. Di Francesco, *ACS Appl. Mater. Interfaces* **2021**, *13*, 30245.
[43] R. Ye, D. K. James, J. M. Tour, *Adv. Mater.* **2019**, *31*, 1803621.
[44] J. Lin, Z. Peng, Y. Liu, F. Ruiz-Zepeda, R. Ye, E. L. Samuel, M. J. Yacaman, B. I. Yakobson, J. M. Tour, *Nat. Commun.* **2014**, *5*, 5714.
[45] Y. Chyan, R. Ye, Y. Li, S. P. Singh, C. J. Arnusch, J. M. Tour, *ACS Nano* **2018**, *12*, 2176.
[46] H. Li, T. Chang, Y. Gai, K. Liang, Y. Jiao, D. Li, X. Jiang, Y. Wang, X. Huang, H. Wu, Y. Liu, J. Li, Y. Bai, K. Geng, N. Zhang, H. Meng, D. Huang, Z. Li, X. Yu, L. Chang, *Nano Energy* **2022**, *92*, 106786.
[47] M. Chung, G. Fortunato, N. Radacsi, *J. R. Soc., Interface* **2019**, *16*, 20190217.
[48] P. Pirovano, M. Dorrian, A. Shinde, A. Donohoe, A. J. Brady, N. M. Moyna, G. Wallace, D. Diamond, M. McCaul, *Talanta* **2020**, *219*, 121145.